Relativistic electron energy loss spectroscopy of solid and core-shell nanowires

J. K. Hyun[*]

Department of Physics, Cornell University, Ithaca, New York 14853, USA

M. P. Levendorf, M. Blood-Forsythe, and J. Park
Department of Chemistry and Chemical Biology, Cornell University, Ithaca, New York 14853, USA

D. A. Muller
Department of Applied and Engineering Physics, Cornell University, Ithaca, New York 14853, USA

Near-field optical spectroscopy with nanometer spatial resolution using transition radiation from a focused, relativistic electron beam is demonstrated for Ge nanowires. The excitation of the waveguide modes is absent in theoretical treatments that neglect retardation because the coupling of the swift electron to the optical modes of the nanowire is a consequence of its relativistic nature. Here, relativistic energy loss probabilities for aloof electron trajectories near a perpendicularly oriented single nanowire are analytically calculated using a local dielectric theory. Multimode and zero-mode Ge nanowires are experimentally measured in this geometry with a ~2-nm-size electron probe. Observations fall in excellent agreement with the retarded calculations. Optical eigenmodes are identified from comparison of the experimental electron energy loss spectra to theoretical dispersion maps. Adding a Drude-type metallic shell to a dielectric nanowire provides surface-plasmon modes in the same energy range as the dielectric waveguide, leading to strongly coupled hybrid modes that can be efficiently excited by the incident electron. Such results demonstrate a powerful solution for optical studies of nanosystems with nanometer spatial resolution over a broadband energy range.

I. INTRODUCTION

Single nanowires have been demonstrated as building blocks for optoelectronic devices[1] including sensors[2] and nanolasers[3,4] while core-shell nanowire systems have shown promise as functional solar cells[5,6] and optical antennas.[7] Improvements in nanowire integrated optoelectronic device performance rely heavily on understanding the optical properties. However, the experimental task of measuring the optical modes of a nanoscale structure with conventional optical techniques can be challenging because while spatial resolution commensurate with the underlying modes is necessary, diffraction limitations often restrict this possibility. Optical techniques such as the scanning near-field optical microscope (SNOM) circumvent this problem by directly detecting the near-field intensities with a waveguide probe, but the resolution is determined by the aperture size, typically ~50 nm at best. The aperture size can be reduced, but at a very significant cost to the signal. While electrons can be focused down to sub-nm probe sizes using electromagnetic lenses, until recently, there have been practical challenges in recording losses at optical frequencies. Nanometer resolution is easily achieved with scanning transmission electron microscopy (STEM), where spatial resolution limitations arise from aberrations in the electromagnetic lenses, removable with the implementation of correctors. Furthermore, as the electron is accelerated to velocities typically exceeding half the speed of light ($v/c > 0.5$), it behaves as a broad-band source of light.[8] The relativistic speed allows the Fourier components of the field of the fast electron to extend across a broad energy range with a maximum frequency order roughly corresponding to $\omega \sim \gamma v / b$, where b is the electron's distance to its scatterer, v is its velocity, and γ is the relativistic factor.

Electron energy loss spectroscopy (EELS) below 50 eV, or the low-loss regime, is typically associated with valence excitations. Experimentally high signal-to-noise ratios are achieved compared to the core-loss energies, but the interpretation is less straightforward. It is in this energy range that optical responses of the target can be correlated to the energy loss spectrum through a dielectric formalism. A continuum theory employing a macroscopic dielectric function permits the description of interband transitions, plasmon excitations, and radiative losses from EELS.[9] Early studies of radiative optical surface modes in thin films[10,11] and small metallic particles[12] have demonstrated this ability. Moreover, recent developments in the stability of the electron source through monochromation have improved energy resolution and allowed detection of modes with lifetimes on the order of 100 meV. This has also made the infrared-visible energy range more accessible through the reduction of the zero-loss peak tails, generated by the tails of the primary beam. Studies on Cherenkov radiation in Si-based nanocomposites[13] and delocalization in ultrathin gate stacks[14] have directly benefited from this instrumental improvement.

There have been numerous studies linking EELS to nanowires in the nonrelativistic framework where retardation is neglected. Energy loss probabilities for nonpenetrating electrons normally incident near solid and hollow nanowires were theoretically investigated by Bertsch *et al.*[15] The formalism was extended by Zabala *et al.* to include penetrating trajectories.[16] Nanowires with anisotropic dielectric functions were also considered by Taverna *et al.*[17] In the limit of slow electron velocities or small wire diameters, the nonretarded treatment should suffice for the description of energy loss probabilities. However, it is also questionable of whether a dielectric-continuum approach is even valid in the

limit of small sizes as quantum-mechanical corrections may be necessary.[17,18] For larger diameters where the valence band behaves as a continuum, a dielectric formalism is well justified. For diameters exceeding the mode wavelength ($a > \lambda$) and with relativistic electron velocities, retardation effects can dominate, introducing the need for a relativistic treatment. This requirement is further strengthened from a practical standpoint as optoelectronic devices typically employ nanowires of diameters greater than 50 nm to match the optical wavelength.

Relativistic formalisms for spheres,[19] semi-infinite solids,[20] stratified layers,[21] and nanowires probed along the direction of the cylindrical axis[22,23] have been previously addressed. Experimental evidence for whispering gallery modes in silica nanospheres probed by aloof electrons was shown in an earlier work.[24] However, there has not yet been a relativistic study of solid and core-shell nanowires probed at normal incidence with aloof electrons. The boundary element method (BEM) developed by García de Abajo and Howie permits the calculation of energy loss probabilities of various geometries using surface discretization.[25,26] An analytical derivation dedicated to our system of interest, however, benefits from the direct generation of a dispersion map of the electron energy loss, especially useful for correlating spectroscopic features to the optical eigenmodes.

Two main energy loss mechanisms due to the relativistic interaction of a fast charged particle and target are categorized as Cherenkov or transition radiation.[8] Cherenkov radiation originates from the coherent interference of shock waves created from the charged particle moving at speeds exceeding the speed of light in the medium. Transition radiation is conventionally referred to as radiation emitted from the fast particle traversing two different mediums, resulting from the rearrangement of the field distribution. Often considered to be parasitic in nature, transition radiation can be useful in identifying optical eigenmodes of the target structure.[24] When the wavelength of radiation is able to form a standing wave inside the characteristic dimension of the structure, a coherent far-field response is created, which interacts with the electron and results in its energy loss.

In this paper, we expand the field of the electron in vector cylindrical harmonics and derive an analytical expression of the relativistic energy loss probability for a fast electron normally incident near an infinite wire. We compare calculations to experimental results on single Ge nanowires, where excellent agreement is found. Two diameters, representing a zero-mode and multimode waveguides, are studied.

We also consider core-shell dielectric-metal nanowires which have gained substantial attention due to their interesting optical properties. Most notably, the ability to tune the surface-plasmon resonance[27] has found a range of biological and photonic applications.[28] A simple intuitive picture explaining the dipolar surface-plasmon resonances due to the interaction of the inner and outer surfaces of core-shell spheres was developed by Prodan *et al.*[29] in the dipole limit. The evolution of optical fields inside larger diameters was also studied by Penninkhof *et al.*[30] From electron energy loss, we also demonstrate the qualitative behavior of the dipolar plasmon resonances, the effect of different dielectric cores, and the interaction between the dielectric waveguide mode and surface plasmon.
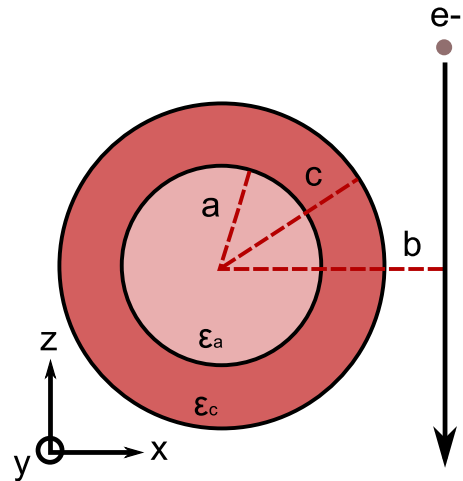

FIG. 1. (Color online) Geometry of the experiment. The core-shell nanowire extends along the y axis and consists of an inner core of radius a, described by the dielectric function ϵ_a, while the outer shell extends to radius c, described by ϵ_c. The aloof electron travels parallel to the z axis and passes closest to the wire at a distance b from the center of the wire.

II. RELATIVISTIC EELS FOR SOLID AND CORE-SHELL NANOWIRES

The system consists of an infinite wire of inner radius a and outer radius c (Fig. 1) extending along the y axis. The wire is positioned in vacuum (i.e., $\epsilon = 1$) and the core and shell are characterized by frequency-dependent dielectric functions, ϵ_a and ϵ_c, respectively. The wire is considered to be nonmagnetic (i.e., $\mu = 1$). An electron travels in vacuum at relativistic speeds, v, parallel to the z axis, and impinges near the surface of the wire. The nearest distance from the center of the wire to the path of the electron is along the x axis and is described by the impact parameter, b.

The treatment of the problem is analogous to the case for a spherical target derived by García de Abajo.[19] The external field associated with the fast electron as it traverses near the wire is first expanded in terms of vector cylindrical harmonics. The interaction between this field and the wire is expressed as a scattering problem where the scattering matrix is determined from solutions to the boundary conditions. The energy loss probability is then calculated from the work done on the electron as it experiences a retarding force from the scattered field.

A. Vector harmonics and scalar functions

To expand the electric field in terms of cylindrical harmonics, we can define the operator $\vec{S} = -i\hat{y} \times \vec{\nabla}$. This is analogous to $\vec{L} = -i\vec{r} \times \vec{\nabla}$ used as the angular-momentum operator to generate spherical harmonics.[19] $\vec{S}$ in polar or Cartesian coordinates takes the following forms:

$$\vec{S} = \frac{1}{i}\left(-\frac{\hat{r}}{r}\frac{\partial}{\partial\phi} + \hat{\phi}\frac{\partial}{\partial r}\right) \tag{1}$$

or

$$\vec{S} = \frac{1}{i}\left(\hat{x}\frac{\partial}{\partial z} - \hat{z}\frac{\partial}{\partial x}\right). \tag{2}$$

Using this operator, the external and scattered fields can be expressed as

$$\vec{E}^{\alpha} = \vec{S}\Psi_{\perp}^{\alpha} - \frac{i}{k}\vec{\nabla}\times\vec{S}\Psi_{\parallel}^{\alpha}, \tag{3}$$

$$\vec{H}^{\alpha} = -\frac{i}{k}\vec{\nabla}\times\vec{S}\Psi_{\perp}^{\alpha} - \vec{S}\Psi_{\parallel}^{\alpha}, \tag{4}$$

where $k = \omega/c$ and α refers to the external or scattered fields, respectively, labeled "ext" or "sct." From Eq. (3),

$$\Psi_{\perp}^{\alpha} = \frac{\vec{S}\cdot\vec{E}^{\alpha}}{\vec{S}\cdot\vec{S}} \tag{5}$$

describes the scalar function associated with the electric field component polarized perpendicular to the cylindrical axis and

$$\Psi_{\parallel}^{\alpha} = \frac{i}{k}\frac{(\vec{S}\times\vec{\nabla})\cdot\vec{E}^{\alpha}}{\vec{S}\cdot\vec{S}} \tag{6}$$

describes the scalar function associated with the electric field component polarized parallel to the cylindrical axis. For the field inside the wire, the fields can be described as

$$\vec{E}^{\mathrm{int}} = \vec{S}\Psi_{\perp}^{\mathrm{int}} - \frac{i}{\epsilon_{\zeta}k}\vec{\nabla}\times\vec{S}\Psi_{\parallel}^{\mathrm{int}}, \tag{7}$$

$$\vec{H}^{\mathrm{int}} = -\frac{i}{k}\vec{\nabla}\times\vec{S}\Psi_{\perp}^{\mathrm{int}} - \vec{S}\Psi_{\parallel}^{\mathrm{int}}, \tag{8}$$

where ζ refers to the core ($\zeta = a$) or shell ($\zeta = c$).

B. Scattering matrix

The case of a solid wire (i.e., $\epsilon_c = 1$) is first considered. The interaction between the external fields of the fast electron and the scattered field due to the nanowire is contained in the scattering matrix. The external field of the fast electron can be expressed as

$$\Psi_l^{\mathrm{ext}}(\vec{x}) = \frac{i}{2}\sum_m e^{im\phi}\int dg e^{igy}J_m(ur)\Psi_{gml}^{\mathrm{ext}}, \tag{9}$$

where l indicates the polarization ($\perp$ or $\parallel$), g is the axial propagation constant, $u = \sqrt{k^2 - g^2}$, and $\Psi_{gml}^{\mathrm{ext}}$ is the expansion coefficient. The derivation of $\Psi_{gml}^{\mathrm{ext}}$ is outlined in Appendixes A and B. The forms for Ψ_l^{sct} describing the scattered fields can be found by choosing the well-behaved Bessel function at $r\to\infty$. We find that

$$\Psi_l^{\mathrm{sct}}(\vec{x}) = \frac{i}{2}\sum_m e^{im\phi}\int dg e^{igy}H_m^{(1)}(ur)\Psi_{gml}^{\mathrm{sct}}. \tag{10}$$

For the internal fields, $\Psi_l^{\mathrm{int}}\sim J_m(u_a r)$, where $u_a = \sqrt{\epsilon_a k^2 - g^2}$ is necessary to satisfy the wave equation inside the dielectric,

$(\nabla^2 + \epsilon_a k^2)\Psi^{\mathrm{int}} = 0$. The scattered field expansion coefficients can be written as

$$\begin{pmatrix}\Psi_{gm\perp}^{\mathrm{sct}}\\\Psi_{gm\parallel}^{\mathrm{sct}}\end{pmatrix} = \begin{pmatrix}a_{m\perp} & a_{m\parallel}\\b_{m\perp} & b_{m\parallel}\end{pmatrix}\begin{pmatrix}\Psi_{gm\perp}^{\mathrm{ext}}\\\Psi_{gm\parallel}^{\mathrm{ext}}\end{pmatrix}, \tag{11}$$

where the matrix elements are described in Appendix C. For the core-shell nanowire, the Bessel function inside the scalar function describing the shell region ($a < r < c$) is a linear combination of $J_m(u_c r)$ and $Y_m(u_c r)$, where $u_c = \sqrt{\epsilon_c k^2 - g^2}$. Again, the boundary conditions for the electric and magnetic fields are satisfied and extensive algebra generates an analytical solution for the scattering matrix elements (see Appendix D).

C. Energy loss

The energy loss experienced by an electron due to the scattered field can be written as

$$E^{\mathrm{loss}} = \int_0^{\infty}\omega d\omega\Gamma^{\mathrm{loss}}(\omega), \tag{12}$$

where

$$\Gamma^{\mathrm{loss}}(\omega) = \frac{1}{\pi\omega}\int dt\, \mathrm{Re}\{e^{-i\omega t}\vec{v}\cdot\vec{E}^{\mathrm{sct}}(\vec{x_t},\omega)\} \tag{13}$$

represents the energy loss probability. Inserting Eq. (3) for the scattered electric field, we find

$$\Gamma^{\mathrm{loss}}(\omega) = \frac{1}{\pi\omega}\int dt\, \mathrm{Re}\left\{e^{-i\omega t}\left(\vec{v}\cdot\vec{S}\Psi_{\perp}^{\mathrm{sct}} - \frac{i}{k}\vec{v}\cdot(\vec{\nabla}\times\vec{S})\Psi_{\parallel}^{\mathrm{sct}}\right)\right\}, \tag{14}$$

where

$$\Psi_{\perp}^{\mathrm{sct}}(\vec{x_t}) = \frac{i}{2}\sum_m e^{im\phi_t}\int dg e^{igy_t}H_m^{(1)}(ur_t)(a_{m\perp}\Psi_{gm\perp}^{\mathrm{ext}} + a_{m\parallel}\Psi_{gm\parallel}^{\mathrm{ext}}), \tag{15a}$$

$$\Psi_{\parallel}^{\mathrm{sct}}(\vec{x_t}) = \frac{i}{2}\sum_m e^{im\phi_t}\int dg e^{igy_t}H_m^{(1)}(ur_t)(b_{m\perp}\Psi_{gm\perp}^{\mathrm{ext}} + b_{m\parallel}\Psi_{gm\parallel}^{\mathrm{ext}}) \tag{15b}$$

are obtained from Eqs. (10) and (11). Applying the results from Eqs. (A6), (B5), and (B8), we can then express the energy loss in its final form

$$\Gamma^{\mathrm{loss}}(\omega) = \int dg S(g,\omega), \tag{16}$$

where

$$S(g,\omega) = \frac{1}{\pi}\sum_m \mathrm{Re}\left\{\frac{1}{2u^2}(-\beta^2\lambda^2 a_{m\perp} + i\beta g\lambda a_{m\parallel} - i\beta g\lambda b_{m\perp} - g^2 b_{m\parallel})|\Psi_{gm}(\vec{x_0})|^2\right\} \tag{17}$$

and

$$|\Psi_{gm}(\vec{x}_0)|^2 = \frac{4}{v^2}\frac{e^{-2b\lambda}}{\lambda^2}\left(\frac{\lambda+\omega/v}{u}\right)^{2m}. \tag{18}$$

Here, $\beta = v/c$, $\lambda = \sqrt{g^2+(\omega/v\gamma)^2}$. The first three terms in Eq. (17) have prefactors of β^2 or β, thereby tending to zero for a slow incident electron. Thus the form of the loss function and excitations of the cylinder that are probed for fast and slow electrons will be very different. The dependence of the impact parameter on the energy loss is described by Eq. (18), where an exponential decay is associated with increasing b.

It is instructive to see the energy loss probability Γ^{loss} at the nonrelativistic limit (i.e., $c\to\infty$), in which case $\beta\to 0$. Likewise, $u=u_a=ig$, which follows from $k\to 0$, and the Bessel functions take the form of modified Bessel functions allowing Eq. (C6) to be rewritten as

$$b_{m\parallel} = (-1)^m\frac{i\pi}{2}\frac{\epsilon_a I'_m(ga)I_m(ga)-I'_m(ga)I_m(ga)}{I_m(ga)K'_m(ga)-\epsilon_a I'_m(ga)K_m(ga)}. \tag{19}$$

The energy loss in the nonrelativistic limit is then expressed as

$$\Gamma^{\text{loss}}(\omega) = \frac{2}{\pi v^2}\sum_m \text{Re}\left\{\int dg(-1)^m b_{m\parallel}\right.$$
$$\left.\times\frac{\exp(-2b\lambda_{nr})}{\lambda_{nr}^2}\left(\frac{\lambda_{nr}+\omega/v}{g}\right)^{2m}\right\}, \tag{20}$$

where $\lambda_{nr}=\sqrt{g^2+(\omega/v)^2}$. Equation (20) is equivalent to the Bertsch formalism[15] provided it undergoes a conversion to atomic units (i.e., $e=\hbar=1$). The fact that only the term involving $b_{m\parallel}$ in Eq. (17) survives in the nonrelativistic limit has some physical interpretation. $b_{m\parallel}$ describes the interaction of the polarization parallel to the cylindrical axis. Effects of retardation appear when the dimension of the structure is on the order of the wavelength. Because the wire is considered to be infinite in the parallel direction, the axial dimension is never exceeded by the wavelength. On the other hand, the three lost terms in Eq. (17) describe the interaction of the perpendicular polarization and the intermixing of polarizations from parallel to perpendicular and vice versa. In this case, the dimension in the perpendicular direction is constrained by the diameter of the wire. Retardation therefore plays a more significant role for these terms, manifested by the presence of the relativistic prefactor β.

III. EXPERIMENTS AND ANALYSIS

Samples were prepared for nanowire growth by depositing gold nanoparticles using a process previously reported by Woodruff *et al.*[31] Silicon substrates were briefly etched in dilute hydroflouric acid (HF) ($<2\%$) in order to remove the native oxide. One part dilute HF was then added to nine parts of 200 nm gold nanoparticle solution (Ted Pella) and the resultant mixture was then placed onto the substrate. After being blown dry under N_2, samples were immediately transferred to a tube reactor chemical vapor deposition system and heated to growth temperature under argon flow. Growths were performed for 12 min at 320 °C and a constant pressure of 200 Torr. Germane (1.46% in hydrogen) was used as
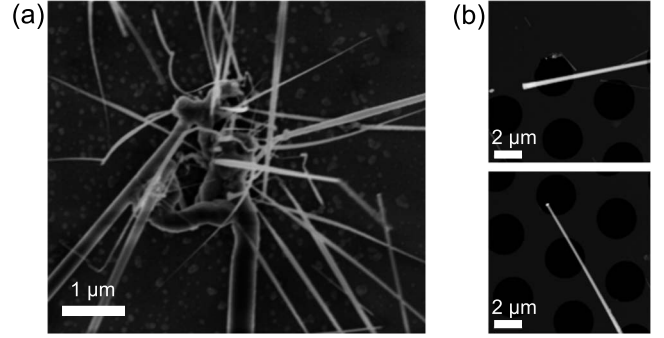

FIG. 2. (a) Scanning electron microscopy (SEM) image of Ge wires grown on a Si substrate. (b) High-angle annular dark field STEM images of individual Ge nanowires dispersed on perforated SiN_x films.

the source gas and was further diluted in hydrogen in order to maintain a partial pressure of 2.34 Torr. Samples were subsequently annealed under 30 Torr of hydrogen at the growth temperature for 10 min and then cooled under vacuum. Figure 2(a) shows the as-grown nanowires on a silicon wafer. The nanowires were sonicated in methanol (MeOH) and dispersed onto a SiN_x TEM grid containing an array of 50-μm-size perforated holes (Ted Pella Inc) [see Fig. 2(b)]. Annular dark field (ADF) imaging and EELS measurements of the nanowires were performed on a 200 kV FEI Tecnai F20-ST STEM equipped with a Gatan imaging filter 865-ER. The convergence and collection semiangles were 8 and 12.5 mrad, respectively. The size of the focused probe was around 2 nm. The electrons were filtered through a Wien-filter monochromator, enabling an enhancement in the energy resolution, measured at 130 meV. Long acquisition times for high signal-to-noise ratios were preferable. However, fluctuation in the high tension voltage ranged within 100 meV. Therefore, in order to minimize the degradation of energy resolution due to the instabilities, a series of spectra including the full zero loss peak (ZLP) were acquired at short acquisition times (0.1 s) after which the spectra were aligned through cross correlations and summed. This method generates sufficient statistics for analysis and allows for the identification of the peak energies with respect to the ZLP.

Ge nanowires suspended across the vacuum were investigated, where the probe was stationed $\sim$3 nm away from the surface of the nanowire and sufficiently distanced from the edge of the SiN_x perforated support.

The single crystallinity of the Ge nanowires restricts the cross-sectional geometries to hexagons or octagons instead of a circle. The eigenmodes of the equal-area cylinder set a variational lower bound for the hexagonal cylinder while the eigenmodes of the inscribed cylinder set an upper bound.[32] A comparison of the waveguide modes for hexagonal and circular wires to equal-area cross sections therefore shows good correspondence, especially near lower energies.

In order to account for the tail of the ZLP, a background model consisting of a convolution between a Lorentzian and Gaussian was added to the theory and fitted to the original data through the least-means-squares method. Figure 3 shows the original data for a 286-nm-diameter nanowire and the fitted theory including the background model.
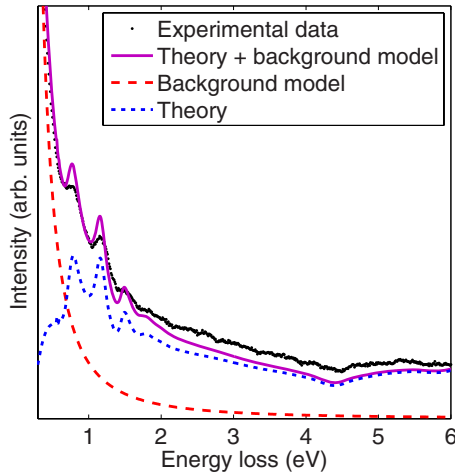
FIG. 3. (Color online) Experimental and simulated EELS for a 286-nm-diameter nanowire. A fitted background model (dashed curve) is added to the theory (short dashed curve) resulting in the solid curve which agrees well with the experiment (dotted curve).

IV. RESULTS AND DISCUSSION

A. Solid nanowires

The frequency-dependent Ge dielectric function of Philipp and Taft[33] was used for our modeling. The function is characterized by a vanishing imaginary component and a large real component below 2 eV (see Fig. 4), indicating minimal absorption and good transmissivity. Near 2 eV, the imaginary component rises rapidly and at 4.44 eV, a peak value corresponding to an interband transition is reached.

Figure 5 shows background-subtracted EELS from nanowires of 286- and 47-nm diameters and the corresponding calculations. The electron trajectory for all cases is set to be 3 nm away from the surface. Good agreement between experimental data and dielectric theory is demonstrated. The spectrum from the 286-nm-diameter wire shows three prominent peaks below 2 eV, located at 0.7, 1.16, and 1.5 eV. Discrepancy in the peak sharpness between calculation and
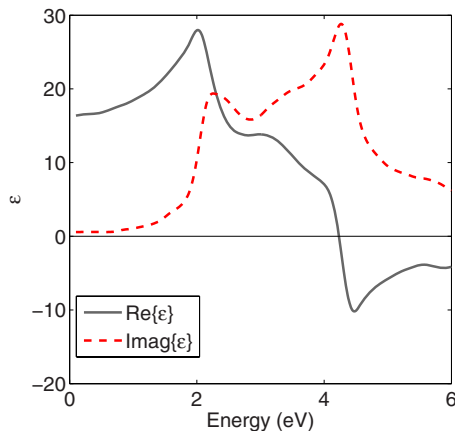

FIG. 4. (Color online) Real and imaginary components of the dielectric function for Ge. The imaginary component decreases to zero below 2 eV indicating negligible optical absorption in this regime.
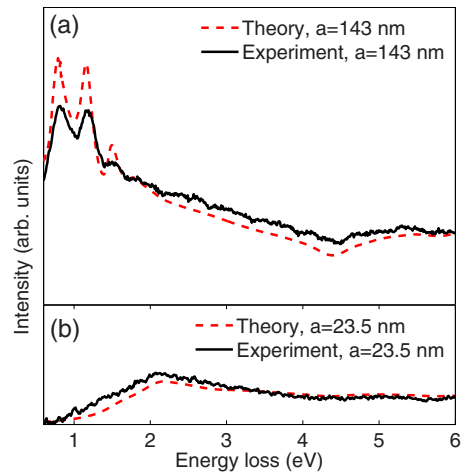

FIG. 5. (Color online) Background-subtracted EEL for 143- and 23.5-nm-radius (or 286- and 47-nm-diameter) wires and the corresponding theory. The fitted background model is subtracted from the raw spectrum. (a) The first three theoretical peaks (dashed curve) in the 286-nm-diameter wire are resolved by experiment (solid curve). (b) The absence of the peaks is shown for the 47-nm-diameter wire for both theory (dashed curve) and experiment (solid curve).

experiment may be attributed to surface roughness or interface states. In both cases, finite absorption results in a slight damping of the peaks. Above 4.44 eV, an edge onset is observable for both theory and experiment, indicative of energy loss to the interband transition. For the 47-nm-diameter wire, the spectrum consists of less intensity relative to the 286-nm-diameter wire and shows an absence of peaks below 2 eV.

Figure 6 provides clearer insight into the origin of the spectra by displaying the dispersion map of the energy loss, described by $S(g, \omega)$ in Eq. (17). Intensity is plotted on a log
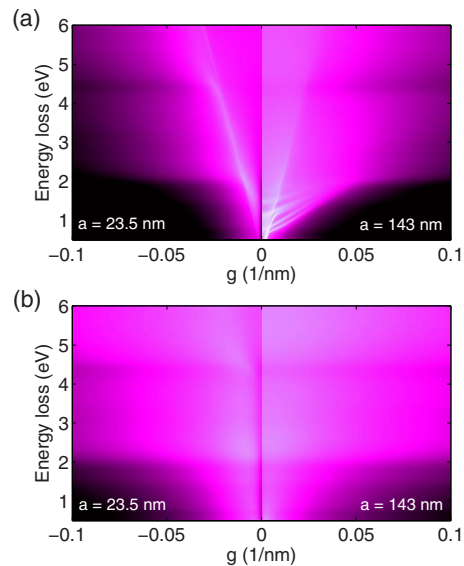

FIG. 6. (Color online) (a) Loss-dispersion map generated from $S(g, \omega)$ for 23.5- and 143-nm-radius (or 47- and 286-nm-diameter) wires. (b) The corresponding nonretarded loss-dispersion map. Intensity is multiplied by 10 for similar contrast. The impact parameter in all cases is 3 nm away from the surface.

scale. Brighter intensity corresponds to stronger coupling between the field of the fast electron and the optical modes of the nanowire. For the 286-nm-diameter wire, the map traces out the optical waveguide modes, characterized by the cylindrically symmetric modes (TM_{0n} and TE_{0n}) and hybrid (HE_{mn}, EH_{mn}) modes. Here, m describes the angular symmetry and n refers to the radial number. The hybrid modes refer to modes that support both electric and magnetic fields in the axial direction. All modes have cutoffs except for the HE_{11} mode. Intensity within and outside the light cone is observed, showing that the field of the electron couples both to the evanescent and propagating modes. In particular, near $g=0$, all terms in Eq. (17) vanish except for the first term involving $a_{m\perp}$. In such case, the modes carry little or no axial momentum and are closely related to the transverse whispering gallery modes whose field distribution is concentrated toward the outer rim of the nanowire. These modes gain momentum by crossing over the light line where they transition into the form of longitudinal propagating modes. The nonzero imaginary dielectric component results in a smooth transition of modes crossing the light line. Above 2 eV and for higher momentum values, the modes are dampened also because of the increased imaginary dielectric component.

For the 47-nm diameter, the nanowire does not support multiple modes. The nanowire acts as a zero-mode waveguide as the lowest-order HE_{11} mode is scaled to higher energies where damping is severe. Weak intensity inside the light-cone shows that radiative effects are less pronounced as in the case for the 286-nm-diameter wire. This can be explained in terms of the formation criterion, where the formation time for coherent radiation to develop must be at least one period. Likewise, the formation length would depend on the characteristic length scale of the target. In the case of the nanowire, the diameter sets the formation criterion. A standing wave is increasingly difficult to form as the diameter of the wire shrinks, inhibiting radiative losses in the light cone.

For comparison, the nonretarded loss map for both diameters is shown in Figure 6(b). The nonretarded intensity was scaled up by a factor of 10 for comparable contrast. The nonretarded loss-dispersion maps for both diameters are similar to one another, but strikingly different compared to the relativistic case in Fig. 6(a). Even for the 47-nm-diameter wire, supporting no mode, the nonretarded map fails to describe any of the characteristic features. Calculations show that for a Ge dielectric function, the nonretarded formalism only coincides with the relativistic formalism for diameters less than ∼1 nm. For slightly larger diameters, although the nonretarded formalism reflects the features of the relativistic formalism, the intensities are different. For example, a 4-nm-diameter Ge wire exhibits a ∼10% difference in its first peak intensity. Even in the size range where both formalisms coincide, caution is necessary in the use of a continuum medium theory as proper consideration of quantum-mechanical effects may be necessary. The nonretarded formalism fails to predict the presence of any of the optical or waveguide modes and thus at diameters large enough to support waveguide modes, the nonretarded formalism also fails qualitatively.

Figure 7 describes the relativistic energy loss probability for nanowire diameters up to 600 nm. For increasing diam-
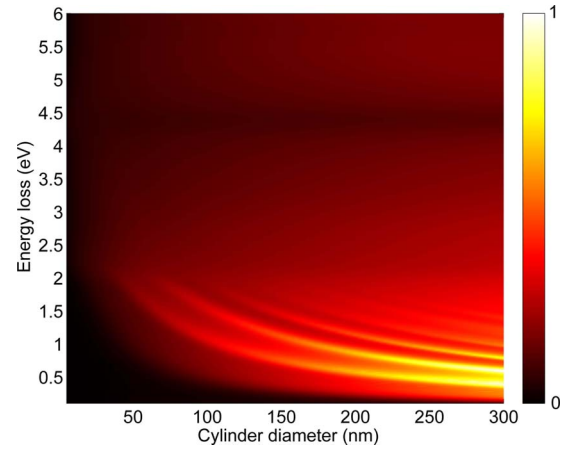

FIG. 7. (Color online) The energy loss probability as a function of diameter. Larger diameters are shown to support a higher density of peaks with improved definition. The increase in intensity above 4.44 eV is indicative of absorption due to the Ge interband transition. The intensities are normalized.

eter, a higher density of peaks is supported, with enhanced sharpness below 2 eV. Peaks are no longer resolved below diameters of ∼50 nm. Here, single modes (HE_{11}) remain, but these modes are strongly dispersed so they do not contribute any peaks when integrated over the momentum, g.

B. Core-shell nanowires

In this section, we calculate the loss-dispersion map of a nanowire consisting of a dielectric core coated by a metallic shell, while the electron again travels perpendicular to the cylindrical axis and passes close to the outer surface of the shell. We first examine the difference between the loss dispersion for a solid and shell wire composed of Au. Both wires share outer diameters of 140 nm. For the shell case, an inner diameter of 130 nm is considered. The fast electron trajectory passes 1 nm away from the outer surface. A realistic dielectric function for Au was interpolated from results by Johnson and Christy.[34] In the energy range of consideration ($1 < E < 3.5$ eV), this dielectric function differs from a simple Drude model in that the imaginary component does not asymptotically approach zero, but instead rises to a finite value above ∼2 eV, resulting in absorption losses. The solid nanowire exhibits surface-plasmon modes described by the $m=0$ mode and a faintly visible $m=1$ mode [Fig. 8(a)]. Here, the $m=1$ mode is severely damped by the finite imaginary component of the dielectric function. For the shell, a drastic difference can be expected in the dispersion of the surface-plasmon modes. The field of the fast electron excites both inner and outer surface-plasmon modes which, at sufficient thicknesses, interact with one another to generate a splitting of each mode into two branches. The high-energy branch is the result of an antisymmetric charge polarization distributed across the two surfaces while the low-energy branch is due to a symmetric charge polarization. Figure 8(a) shows the case of the shell where three clear modes below ∼2 eV originate from the symmetric branches of the $m=0$, $m=1$, and $m=2$ modes. The antisymmetric branches would be supported at
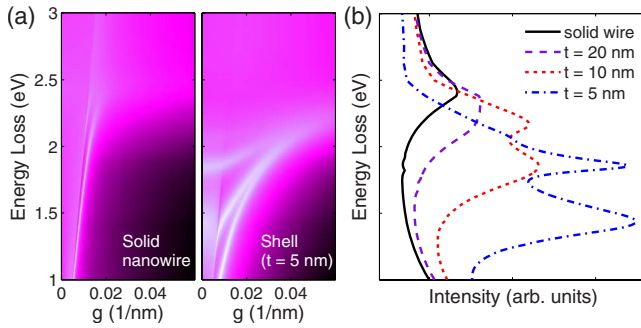
FIG. 8. (Color online) (a) Loss-dispersion maps for a solid 140-nm-diameter Au nanowire and for a Au shell consisting of inner and outer diameters of 130 and 140 nm, respectively. In the case of the shell, the first three modes are due to the lower-energy (or symmetric) branches of the surface plasmonic modes and can be identified from bottom to top as $m=0$, $m=1$, and $m=2$ modes. (b) EELS for different shell thicknesses, t, with the outer diameter fixed at 140 nm. The splitting of the peak originates from the $m=1$ and $m=2$ symmetric modes. Intensity is enhanced for thinner shells as the coupling strength between the inner and outer surfaces increase.

energies higher than ~ 2 eV, but are damped out due to absorption losses.

Figure 8(b) shows the electron energy loss probabilities for different shell thicknesses. In each case, the outer diameter is fixed at 140 nm while the inner diameter is varied. Calculations show that the single peak near 2.5 eV originating from the solid nanowire increases in intensity and splits into two peaks with wider energy separations as the shell grows thinner. In addition, the maximum intensity is redshifted. There exists the possibility of interpreting the two peaks as the result of antisymmetric and symmetric modes at first glance, but Fig. 8(a) demonstrates that they originate from the lower-energy (or symmetric) branches of the $m=1$ and $m=2$ modes. As the shell thickness increases, the field of the fast electron is increasingly shielded from the inner surface, while the coupling strength weakens due to the increased separation between inner and outer surfaces. Moreover, from Bohr's adiabatic criterion ($b \sim v/\omega$), which estimates the impact parameter required to couple to an excitation, ω, the increase in mode energies for thicker shells allows the same impact parameter to excite the surface plasmons less efficiently, therefore reducing the intensity.

The influence of a dielectric core is illustrated in Fig. 9. Here, we use two different dielectrics that exhibit a wide optical band gap such that absorption in the energy range less than the band gap can be minimized. SiO_2 and GaN both provide negligible imaginary dielectric components in the energy range of interest. The inner diameter of the shell is 160 nm, the outer diameter is 200 nm, and the fast electron travels 1 nm away from the outer surface. For a shell consisting of vacuum, no apparent splitting is observable from the loss spectrum. Similar to the $t=20$ nm case in Fig. 8(b), the shell thickness effectively shields the penetrating electric field from exciting the inner surface plasmons. However, for a shell of the same thickness, inclusion of a dielectric core alters the behavior of the loss spectrum drastically through the introduction of energy shifts and splitting of peaks. Intuitively, the dielectric near the surface becomes polarized by
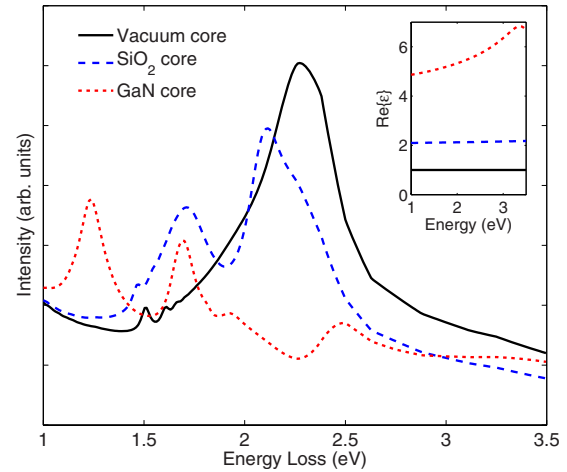
FIG. 9. (Color online) EELS for a Au shell consisting of inner and outer diameters of 160 and 200 nm, respectively. Different dielectric cores result in the shifting and splitting of energies depending on their dielectric constant. Inset shows only the real part of the dielectric constants for SiO_2 and GaN as the imaginary component is small in the energy range of consideration ($1<E<3.5$ eV).

the shell, causing a reduction in the effective surface charge of the metal. This reduces the energy required to excite the surface plasmons on the inner surface. The inset in Fig. 9 describes the real part of the dielectric function for vacuum, SiO_2, and GaN cores, respectively. For higher values of the real dielectric constant, the general collection of peaks is shifted to lower energies. Figure 10 illustrates this behavior more clearly through the loss-dispersion map, where the lower-order modes are increasingly pushed down in energy for dielectrics carrying a higher index. For the GaN core, the symmetric branches of the first three lowest-order modes can be resolved. The antisymmetric branch of the $m=0$ mode is faintly visible near 2.5 eV and shows dispersion characteristics near the light line.

For simple illustration purposes, a Drude model for Au is considered, where above 2 eV, the imaginary component of the dielectric function asymptotically approaches zero. We consider a 160-nm-diameter GaN core surrounded by a 5-nm-thick shell of Au whose dielectric function can be described by[30]

FIG. 10. (Color online) The loss-dispersion maps for the same system considered in Fig. 9. The gradual redshift of the symmetric modes occurs for higher dielectric constants.

FIG. 11. (Color online) Loss-dispersion maps for a GaN core, a Drude-model Au shell, and the combined system. Only the $m=1$ mode is considered for illustration purposes. The core diamete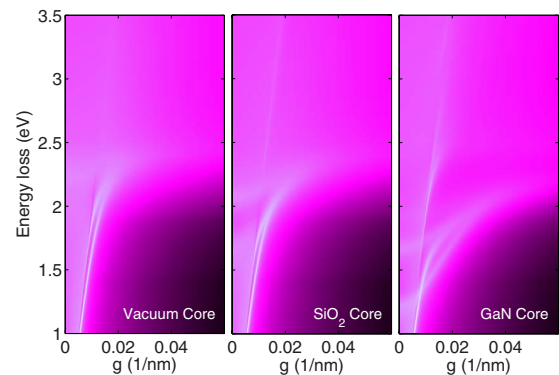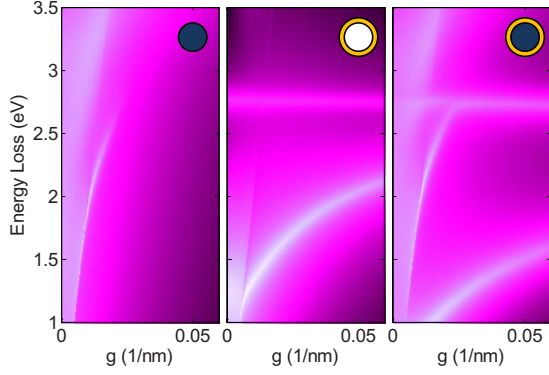r is 160 nm and the outer-shell diameter is 170 nm. The impact parameter in all cases is 1 nm away from the outer shell (or 6 nm away from the core). The HE_{11} mode apparent in the isolated GaN core converges to the antisymmetric mode from the Drude-type Au shell.

$$\epsilon_{Au}(\omega) = \epsilon_d - \frac{\omega_p^2}{\omega^2 + i\omega\gamma_d}, \tag{21}$$

where $\epsilon_d=9.54$, $\omega_p=8.5566$ eV, and the damping factor γ_d $=0.0823$ eV. The impact parameter is 1 nm away from the surface of the outer shell. Only the $m=1$ modes of the system are considered for simplicity. Figure 11 shows the $m=1$ loss dispersion for a GaN core, a Drude-model Au shell, and the combined core-shell system. The impact parameter for the solid core is 6 nm away from its surface. The dispersion for the shell-free GaN core exhibits the HE_{11} waveguide mode. For the case of a Au shell with a vacuum core, the loss-dispersion map shows the splitting of the $m=1$ mode into its symmetric and antisymmetric branches, where the fairly dispersionless antisymmetric branch was previously damped out using a realistic dielectric function for Au. The introduction of the GaN core shows the interesting coupling between modes from the dielectric and metal, where the HE_{11} mode intersects and converges into the antisymmetric $m=1$ mode. This suggests that the HE_{11} mode transforms into a surface-guided mode traveling along the interface between the core and shell. The interaction enhances the intensity of the hybrid mode and implies enhanced optical wave-guiding properties.

V. CONCLUSION

A relativistic formalism in the local dielectric approximation was analytically derived to describe the retarded energy loss probabilities of an aloof electron normally incident to the cylindrical axis of a nanowire. Experimental results on Ge nanowires show a clear departure from the nonretarded theory even at zero-mode waveguide diameters and demonstrate good agreement with the retarded theory. The fast electron permits the detection of optical eigenmodes both inside and outside the light cone, where propagating and evanescent modes contribute to the loss spectrum. In the retarded regime, the waveguide dispersion characteristics are determined by the diameter and dielectric function of the nanowire. We interpret the loss mechanism as similar to transition radiation where the formation criterion is determined by the diameter of the nanowire.

For Au shell nanowires, calculations show EELS detecting the splitting of surface-plasmon modes into antisymmetric and symmetric modes and enhanced loss probabilities for reduced shell thicknesses. Introducing a dielectric core decreases the energy of the symmetric modes. A fictional Au dielectric function using a Drude model was used to illustrate the interaction between the single HE_{11} mode in a GaN core and the antisymmetric $m=1$ mode from the shell, where convergence of the two modes suggests the formation of an optically enhanced hybrid waveguide mode.

As solid and core-shell nanowires are increasingly implemented into optoelectronic devices, detailing the plasmonic and dielectric responses with nanometer-size spatial resolution is of substantial interest. This study presents a powerful near-field solution, demonstrating the optical properties of solid dielectric nanowires and core-shell dielectric-metal nanowires through monochromated STEM and EELS. Because the concept of using relativistic losses to observe the optical eigenmodes is general, the technique can be applied to a wider range of structures including arrays and other complex geometries.

APPENDIX A: EXTERNAL FIELD OF THE FAST ELECTRON

We can describe the electric field of the moving electron as[8,18]

$$\vec{E}^{ext}(\vec{x}) = \left(\vec{\nabla} - \frac{ik\vec{v}}{c}\right)\Phi^{ext}(\vec{x},\omega), \tag{A1}$$

where

$$\Phi^{ext}(\vec{x},\omega) = \int dt e^{\pm i\omega t}G(\vec{x},\vec{x}_t) \tag{A2}$$

and $G(\vec{x},\vec{x}_t)$ is the Green's function for the wave equation $[(\nabla^2+k^2)G=0]$,

$$G(\vec{x},\vec{x}_t) = \frac{e^{ik|\vec{x}-(b,0,vt)|}}{|\vec{x}-(b,0,vt)|}. \tag{A3}$$

The Green's function can be expanded in terms of cylindrical harmonics as

$$G(\vec{x},\vec{x}_t) = \frac{i}{2}\sum_m e^{im(\phi-\phi_t)}\int_{-\infty}^{\infty} dg e^{ig(y-y_t)}H_m^{(1)}(ur_t)J_m(ur), \tag{A4}$$

where g is the axial propagation constant, $u=\sqrt{k^2-g^2}$, and $r<r_t$. $H_m^{(1)}(ur_t)$ is a Bessel function of the third kind defined

by $H_m^{(1)}(x) = J_m(x) + iN_m(x)$. Substituting the cylindrical harmonics expansion of the spherical wave Eq. (A4) into Eq. (A2), we find

$$\Phi^{\text{ext}}(\vec{x}, \omega) = \frac{i}{2} \sum_m e^{im\phi} \int_{-\infty}^{\infty} dg\, e^{igy} J_m(ur) \Psi_{gm}(\vec{x_0}), \quad \text{(A5)}$$

where

$$\Psi_{gm}(\vec{x_0}) = \int dt\, e^{i\omega t} e^{-im\phi_t} e^{-igy_t} H_m^{(1)}(ur_t). \quad \text{(A6)}$$

It is $\Psi_{gm}(\vec{x_0})$ which will describe the expansion coefficients of the moving electron's field. In order to find $\Psi_{gm}(\vec{x_0})$, we can rewrite Eq. (A5) as

$$\Psi_{gm}(\vec{x_0}) = -\frac{2i}{(2\pi)^2 J_m(ur)} \Phi_{gm}^{\text{ext}}(r, \omega), \quad \text{(A7)}$$

where

$$\Phi_{gm}^{\text{ext}}(r, \omega) = \int_0^{2\pi} \int_{-\infty}^{\infty} d\phi\, dy\, e^{-im\phi} e^{-igy} \Phi^{\text{ext}}(\vec{x}, \omega). \quad \text{(A8)}$$

In short, $\Phi_{gm}^{\text{ext}}(r, \omega)$ is the cylindrical representation of $\Phi^{\text{ext}}(\vec{x}, \omega)$. We return to Eq. (A2) to convert the potential into its cylindrical expansion. We can start from[8]

$$\Phi^{\text{ext}}(\vec{k}, \omega) = \frac{2\delta(\omega - \vec{k} \cdot \vec{v})}{k^2 - \frac{\omega^2}{c^2}}, \quad \text{(A9)}$$

which is the spatial Fourier transform of the potential. Taking the spatial Fourier transform of Eq. (A9) in terms of the electron's initial coordinates when $\vec{x}(t=0) = (b, y_0, z_0)$, we obtain

$$\Phi^{\text{ext}}(\vec{x}, \omega) = \frac{e^{i\omega(z-z_0)/v}}{\pi v} \int dk_x dg \frac{e^{ik_x(x-b)} e^{ig(y-y_0)}}{k_x^2 + g^2 + (\omega/v\gamma)^2}. \quad \text{(A10)}$$

The k_x integral is simply

$$\int \frac{e^{ik_x(x-b)}}{k_x^2 + \lambda^2} dk_x = \frac{\pi e^{-|x-b|\lambda}}{\lambda}, \quad \text{(A11)}$$

where $\lambda = \sqrt{g^2 + (\omega/v\gamma)^2}$. Then in the cylindrical (m, g, r) representation, Eq. (A10) becomes

$$\Phi_{gm}^{\text{ext}}(r, \omega) = \frac{2\pi e^{-i\omega z_0/v} e^{-igy_0}}{v} \int_0^{2\pi} d\phi\, e^{-im\phi} e^{i\omega z/v} \frac{e^{-|x-b|\lambda}}{\lambda}. \quad \text{(A12)}$$

$|x-b|$ can be rewritten as $(b-x)$ since the region of interest is where $r < b$. With $x = r \cos\phi$ and $z = r \sin\phi$, Eq. (A12) becomes

$$\Phi_{gm}^{\text{ext}}(r, \omega) = \frac{2\pi e^{-i\omega z_0/v} e^{-igy_0}}{v} \frac{e^{-b\lambda}}{\lambda}$$

$$\times \int_0^{2\pi} d\phi\, e^{-im\phi} e^{i\omega r \sin(\phi)/v} e^{r \cos(\phi)\lambda}. \quad \text{(A13)}$$

The form of the integral has been solved by Bertsch *et al.*[15] without the relativistic factor. Including the relativistic factor, the integral in Eq. (A13) is expressed as

$$\int_0^{2\pi} d\phi\, e^{-im\phi} e^{i\omega r \sin(\phi)/v} e^{r \cos(\phi)\lambda}$$

$$= 2\pi \left(\frac{\lambda + \omega/v}{\sqrt{g^2 - k^2}} \right)^m I_m(r\sqrt{g^2 - k^2}), \quad \text{(A14)}$$

where I_m is the modified Bessel function of the first kind. Combining Eq. (A13) and Eq. (A14) and inserting this into Eq. (A7), we can write $\Psi_{gm}(\vec{x_0})$ as

$$\Psi_{gm}(\vec{x_0}) = \frac{-2i}{v} \frac{e^{-i\omega z_0/v} e^{-igy_0} e^{-b\lambda}}{\lambda} \left(\frac{\lambda + \omega/v}{\sqrt{g^2 - k^2}} \right)^m \frac{I_m(r\sqrt{g^2 - k^2})}{J_m(ur)}. \quad \text{(A15)}$$

However, since $\Psi_{gm}(\vec{x_0})$ needs to be independent of r, we can take the limit of I_m and J_m as $r \to 0$. $\Psi_{gm}(\vec{x_0})$ then is expressed as

$$\Psi_{gm}(\vec{x_0}) = \frac{-2i}{v} \frac{e^{-i\omega z_0/v} e^{-igy_0} e^{-b\lambda}}{\lambda} \left(\frac{\lambda + \omega/v}{u} \right)^m. \quad \text{(A16)}$$

APPENDIX B: THE EXPANSION COEFFICIENTS

Here, the derivation of $\Psi_\perp^{\text{ext}}$ is outlined. We can start with the numerator of Eq. (5)

$$\vec{S} \cdot \vec{E}^{\text{ext}} = \vec{S} \cdot \left(\vec{\nabla} - \frac{ik\vec{v}}{c} \right) \Phi^{\text{ext}}(\vec{x}, \omega). \quad \text{(B1)}$$

We see that $\vec{S} \cdot \vec{\nabla} = 0$ and as the electron travels along the z axis, $\vec{v} = v\hat{z}$, we obtain with Eq. (2)

$$\vec{S} \cdot \vec{E}^{\text{ext}} = \frac{kv}{c} \frac{\partial \Phi^{\text{ext}}(\vec{x}, \omega)}{\partial x}. \quad \text{(B2)}$$

The difficulty with the partial derivative in the Cartesian basis on cylindrical harmonics can be overcome by realizing a trick employing the Green's function.[19] We can observe from Eq. (A3) that the partial derivative of the Green's function with respect to the present position is the negative of the partial derivative with respect to the initial position, (i.e., $\partial/\partial x = -\partial/\partial x_0$). $\Phi^{\text{ext}}(\vec{x}, \omega)$ involves $\Psi_{gm}(\vec{x_0})$ where the initial position, (b, y_0, z_0), is conveniently expressed in Cartesian coordinates. We can now write

$$\vec{S} \cdot \vec{E}^{\text{ext}} = -\frac{ikv}{2c} \sum_m e^{im\phi} \int dg\, e^{igy} J_m(ur) \frac{\partial \Psi_{gm}(\vec{x_0})}{\partial b}. \quad \text{(B3)}$$

The denominator of Eq. (5), $\vec{S} \cdot \vec{S}$, can be obtained working in the cylindrical basis using Eq. (1) and employing the recur-

sive Bessel function identities. $\Psi_\perp^{\mathrm{ext}}$ can now be expressed as

$$\Psi_\perp^{\mathrm{ext}} = \frac{i}{2}\sum_m e^{im\phi}\int dg e^{igy} J_m(ur)\Psi_{gm\perp}^{\mathrm{ext}}, \tag{B4}$$

where the expansion coefficient $\Psi_{gm\perp}^{\mathrm{ext}}$ is

$$\Psi_{gm\perp}^{\mathrm{ext}} = \frac{kv\lambda}{cu^2}\Psi_{gm}(\vec{x_0}). \tag{B5}$$

$\Psi_{gm\|}^{\mathrm{ext}}$ can be found in a similar manner. We can first simplify the numerator of Eq. (6) from

$$\frac{i}{k}(\vec{S}\times\vec{\nabla})\cdot\vec{E} = \frac{i}{k}(\vec{S}\times\vec{\nabla})\cdot\left(\vec{\nabla} - \frac{ik\vec{v}}{c}\right)\Phi^{\mathrm{ext}}(\vec{x},\omega)$$

$$= -\frac{iv}{c}\frac{\partial}{\partial z}\frac{\partial}{\partial y}\Phi^{\mathrm{ext}}(\vec{x},\omega) \tag{B6}$$

by realizing that $(\vec{S}\times\vec{\nabla})\cdot\vec{\nabla}=0$. Again, we can use the trick above for relating the partial derivative of the Green's function with respect to the current position to the initial position. We then obtain

$$\Psi_\|^{\mathrm{ext}} = \frac{i}{2}\sum_m e^{im\phi}\int dg e^{igy} J_m(ur)\Psi_{gm\|}^{\mathrm{ext}}, \tag{B7}$$

where the expansion coefficient $\Psi_{gm\|}^{\mathrm{ext}}$ is

$$\Psi_{gm\|}^{\mathrm{ext}} = -\frac{i\omega g}{cu^2}\Psi_{gm}(\vec{x_0}). \tag{B8}$$

APPENDIX C: SCATTERING MATRIX ELEMENTS FOR A SOLID WIRE

For the case of a solid wire, we assume that the shell is vacuum (i.e., $\epsilon_c=1$). The scattering matrix [Eq. (11)] can be found by imposing the appropriate Maxwell boundary conditions, which require that the tangential components of the electric and magnetic fields be continuous at the boundary of the wire or

$$(\vec{E}^{\mathrm{ext}} + \vec{E}^{\mathrm{sct}} - \vec{E}^a)_{r=a}\times\hat{r} = 0, \tag{C1}$$

$$(\vec{H}^{\mathrm{ext}} + \vec{H}^{\mathrm{sct}} - \vec{H}^a)_{r=a}\times\hat{r} = 0. \tag{C2}$$

With some algebra, we obtain

$$a_{m\perp} = \frac{DC - FA}{FB - EC}, \tag{C3}$$

$$b_{m\perp} = \frac{DB - EA}{FB - EC}, \tag{C4}$$

$$a_{m\|} = \frac{GC - FD}{FB - EC}, \tag{C5}$$

$$b_{m\|} = \frac{GB - ED}{FB - EC}, \tag{C6}$$

where

$$A = ika[u_a^2 u J_m'(ua)J_m(u_aa) - u_a u^2 J_m'(u_aa)J_m(ua)],$$

$$B = ika[u_a^2 u J_m(u_aa)H_m^{'(1)}(ua) - u_a u^2 J_m'(u_aa)H_m^{(1)}(ua)],$$

$$C = mg J_m(u_aa)H_m^{(1)}(ua)(u^2 - u_a^2),$$

$$D = mg J_m(u_aa)J_m(ua)(u_a^2 - u^2),$$

$$E = mg J_m(u_aa)H_m^{(1)}(ua)(u_a^2 - u^2),$$

$$F = ika[u_a^2 u J_m(u_aa)H_m^{'(1)}(ua) - \epsilon_a u_a u^2 J_m'(u_aa)H_m^{(1)}(ua)],$$

$$G = ika[\epsilon_a u_a u^2 J_m'(u_aa)J_m(ua) - u_a^2 u J_m(u_aa)J_m'(ua)].$$

APPENDIX D: SCATTERING MATRIX ELEMENTS FOR A CORE-SHELL WIRE

To solve the matrix elements for the core-shell cylinder, the boundary conditions must be satisfied. This requires the tangential components of the electric and magnetic fields at each interface to be continuous or

$$(\vec{E}^{\mathrm{ext}} + \vec{E}^{\mathrm{sct}} - \vec{E}^c)_{r=c}\times\hat{r} = 0, \tag{D1a}$$

$$(\vec{H}^{\mathrm{ext}} + \vec{H}^{\mathrm{sct}} - \vec{H}^c)_{r=c}\times\hat{r} = 0, \tag{D1b}$$

$$(\vec{E}^c - \vec{E}^a)_{r=a}\times\hat{r} = 0, \tag{D1c}$$

$$(\vec{H}^c - \vec{H}^a)_{r=a}\times\hat{r} = 0. \tag{D1d}$$

Here, $\vec{E}^a$ and $\vec{H}^a$ describe the electric and magnetic fields inside the core while $\vec{E}^c$ and $\vec{H}^c$ describe the fields inside the shell. The scalar functions can be expressed as follows:

$$\Psi_\perp^c = \frac{i}{2}\sum_m e^{im\phi}\int dg e^{igy}\{J_m(u_cr)(c_{m\perp}\Psi_{gm\perp}^{\mathrm{ext}} + c_{m\|}\Psi_{gm\|}^{\mathrm{ext}})$$

$$+ Y_m(u_cr)(d_{m\perp}\Psi_{gm\perp}^{\mathrm{ext}} + d_{m\|}\Psi_{gm\|}^{\mathrm{ext}})\}, \tag{D2a}$$

$$\Psi_\|^c = \frac{i}{2}\sum_m e^{im\phi}\int dg e^{igy}\{J_m(u_cr)(e_{m\perp}\Psi_{gm\perp}^{\mathrm{ext}} + e_{m\|}\Psi_{gm\|}^{\mathrm{ext}})$$

$$+ Y_m(u_cr)(f_{m\perp}\Psi_{gm\perp}^{\mathrm{ext}} + f_{m\|}\Psi_{gm\|}^{\mathrm{ext}})\}, \tag{D2b}$$

$$\Psi_\perp^a = \frac{i}{2}\sum_m e^{im\phi}\int dg e^{igy} J_m(u_ar)(g_{m\perp}\Psi_{gm\perp}^{\mathrm{ext}} + g_{m\|}\Psi_{gm\|}^{\mathrm{ext}}), \tag{D2c}$$

$$\Psi_\|^a = \frac{i}{2}\sum_m e^{im\phi}\int dg e^{igy} J_m(u_ar)(h_{m\perp}\Psi_{gm\perp}^{\mathrm{ext}} + h_{m\|}\Psi_{gm\|}^{\mathrm{ext}}). \tag{D2d}$$

The coefficients c_{ml}, d_{ml}, e_{ml}, and f_{ml} describe the field inside the shell while g_{ml} and h_{ml} describe the field inside the core.

We first consider the case of an external field with parallel polarization [$\vec{E}^{\text{ext}} = -\frac{i}{k}(\nabla \times \vec{S})\Psi_\parallel^{\text{ext}}$ and $\vec{H}^{\text{ext}} = -\vec{S}\Psi_\parallel^{\text{ext}}$]. Equation (D1) is a set of linear equations and can be expressed as

$$\vec{A} \cdot \vec{x_\parallel} = \vec{B_\parallel}, \tag{D3}$$

where $\vec{A}$ is an 8×8 matrix

$$\vec{x_\parallel} = [a_{m\parallel}\ b_{m\parallel}\ c_{m\parallel}\ d_{m\parallel}\ e_{m\parallel}\ f_{m\parallel}\ g_{m\parallel}\ h_{m\parallel}]^T \tag{D4}$$

and

$$\vec{B_\parallel} = \left[-\frac{mg}{kc}J_m(uc)\ \ -u^2 J_m(uc)\ \ iuJ'_m(uc)\ \ 0\ \ 0\ \ 0\ \ 0\ \ 0 \right]^T. \tag{D5}$$

The scattering matrix elements $a_{m\parallel}$ and $b_{m\parallel}$ are the matrix elements relevant to the energy loss probability. These can be found from $\vec{x_\parallel} = \vec{A}^{-1} \cdot \vec{B_\parallel}$. We now consider the case of an external field with perpendicular polarization ($\vec{E}^{\text{ext}} = \vec{S}\Psi_\perp^{\text{ext}}$ and $\vec{H}^{\text{ext}} = -\frac{i}{k}\nabla \times \vec{S}\Psi_\perp^{\text{ext}}$). As before,

$$\vec{A} \cdot \vec{x_\perp} = \vec{B_\perp}. \tag{D6}$$

The vectors $\vec{x_\perp}$ and $\vec{B_\perp}$ are as follows:

$$\vec{x_\perp} = [a_{m\perp}\ b_{m\perp}\ c_{m\perp}\ d_{m\perp}\ e_{m\perp}\ f_{m\perp}\ g_{m\perp}\ h_{m\perp}]^T, \tag{D7}$$

$$\vec{B_\perp} = \left[-iuJ'_m(uc)\ \ 0\ \ -\frac{mg}{kc}J_m(uc)\ \ u^2 J_m(uc)\ \ 0\ \ 0\ \ 0\ \ 0 \right]^T. \tag{D8}$$

The matrix elements $a_{m\perp}$ and $b_{m\perp}$ are found from solving $\vec{x_\perp} = \vec{A}^{-1} \cdot \vec{B_\perp}$. The matrix $\vec{A}$ is

$$\vec{A} = \begin{pmatrix}
iuH_m'^{(1)}(uc) & \frac{mg}{kc}H_m^{(1)}(uc) & -iu_c J'_m(u_c c) & -iu_c Y'_m(u_c c) \\
0 & u^2 H_m^{(1)}(uc) & 0 & 0 \\
\frac{mg}{kc}H_m^{(1)}(uc) & -iuH_m'^{(1)}(uc) & -\frac{mg}{kc}J_m(u_c c) & -\frac{mg}{kc}Y_m(u_c c) \\
u^2 H_m^{(1)}(uc) & 0 & -u_c^2 J_m(u_c c) & -u_c^2 Y_m(u_c c) \\
0 & 0 & iu_c J'_m(u_c a) & iu_c Y'_m(u_c a) \\
0 & 0 & 0 & 0 \\
0 & 0 & \frac{mg}{ka}J_m(u_c a) & \frac{mg}{ka}Y_m(u_c a) \\
0 & 0 & u_c^2 J_m(u_c a) & u_c^2 Y_m(u_c a)
\end{pmatrix}$$

$$\begin{pmatrix}
-\frac{mg}{\sqrt{\epsilon_c}kc}J_m(u_c c) & -\frac{mg}{\sqrt{\epsilon_c}kc}Y_m(u_c c) & 0 & 0 \\
-\frac{u_c^2}{\sqrt{\epsilon_c}}J_m(u_c c) & -\frac{u_c^2}{\sqrt{\epsilon_c}}Y_m(u_c c) & 0 & 0 \\
i\sqrt{\epsilon_c}u_c J'_m(u_c c) & i\sqrt{\epsilon_c}u_c Y'_m(u_c c) & 0 & 0 \\
0 & 0 & 0 & 0 \\
\frac{mg}{\sqrt{\epsilon_c}ka}J_m(u_c a) & \frac{mg}{\sqrt{\epsilon_c}ka}Y_m(u_c a) & -iu_a J'_m(u_a a) & -\frac{mg}{\sqrt{\epsilon_a}ka}J_m(u_a a) \\
\frac{u_c^2}{\sqrt{\epsilon_c}}J_m(u_c a) & \frac{u_c^2}{\sqrt{\epsilon_c}}Y_m(u_c a) & 0 & -\frac{u_a^2}{\sqrt{\epsilon_a}}J_m(u_a a) \\
-i\sqrt{\epsilon_c}u_c J'_m(u_c a) & -i\sqrt{\epsilon_c}u_c Y'_m(u_c a) & -\frac{mg}{ka}J_m(u_a a) & i\sqrt{\epsilon_a}u_a J'_m(u_a a) \\
0 & 0 & -u_a^2 J_m(u_a a) & 0
\end{pmatrix}, \tag{D9}$$

*jkh32@cornell.edu

[1] R. Agarwal and C. M. Lieber, Appl. Phys. A: Mater. Sci. Process. **85**, 209 (2006).

[2] Z. Fan, J. C. Ho, Z. A. Jacobson, H. Razavi, and A. Javey, Proc. Natl. Acad. Sci. U.S.A. **105**, 11066 (2008).

[3] J. C. Johnson, H.-J. Choi, K. P. Knutsen, R. D. Schaller, P. Yang, and R. J. Saykally, Nature Mater. **1**, 106 (2002).

[4] R. Agarwal, C. J. Barrelet, and C. M. Lieber, Nano Lett. **5**, 917 (2005).

[5] B. Tian, X. Zheng, T. J. Kempa, Y. Fang, N. Yu, G. Yu, J. Huang, and C. M. Lieber, Nature (London) **449**, 885 (2007).

[6] B. M. Kayes, H. A. Atwater, and N. S. Lewis, J. Appl. Phys. **97**,

114302 (2005).

[7] J. Li and N. Engheta, IEEE Trans. Antennas Propag. **55**, 3018 (2007).

[8] J. D. Jackson, *Classical Electrodynamics*, 3rd ed. (Wiley, New York, 1998).

[9] Z. L. Wang, Micron **27**, 265 (1996).

[10] R. Vincent and J. Silcox, Phys. Rev. Lett. **31**, 1487 (1973).

[11] C. H. Chen and J. Silcox, Phys. Rev. Lett. **35**, 390 (1975).

[12] P. E. Batson, Phys. Rev. Lett. **49**, 936 (1982).

[13] A. Yurtsever, M. Couillard, and D. A. Muller, Phys. Rev. Lett. **100**, 217402 (2008).

[14] M. Couillard, A. Yurtsever, and D. A. Muller, Phys. Rev. B **77**, 085318 (2008).

[15] G. F. Bertsch, H. Esbensen, and B. W. Reed, Phys. Rev. B **58**, 14031 (1998).

[16] N. Zabala, E. Ogando, A. Rivacoba, and F. J. García de Abajo, Phys. Rev. B **64**, 205410 (2001).

[17] D. Taverna, M. Kociak, V. Charbois, and L. Henrard, Phys. Rev. B **66**, 235419 (2002).

[18] F. Ouyang, P. E. Batson, and M. Isaacson, Phys. Rev. B **46**, 15421 (1992).

[19] F. J. García de Abajo, Phys. Rev. B **59**, 3095 (1999).

[20] R. Garcia-Molina, A. Gras-Martit, A. Howie, and R. H. Ritchie, J. Phys. C **18**, 5335 (1985).

[21] J. P. R. Bolton and M. Chen, J. Phys.: Condens. Matter **7**, 3389 (1995).

[22] C. A. Walsh, Philos. Mag. A **59**, 227 (1989).

[23] N. Zabala, A. Rivacoba, and P. Echenique, Surf. Sci. **209**, 465 (1989).

[24] J. K. Hyun, M. Couillard, P. Rajendran, C. M. Liddell, and D. A. Muller, Appl. Phys. Lett. **93**, 243106 (2008).

[25] F. J. García de Abajo and A. Howie, Phys. Rev. Lett. **80**, 5180 (1998).

[26] F. J. García de Abajo and A. Howie, Phys. Rev. B **65**, 115418 (2002).

[27] C. Graf and A. van Blaaderen, Langmuir **18**, 524 (2002).

[28] M. Brongersma, Nature Mater. **2**, 296 (2003).

[29] E. Prodan, C. Radloff, N. J. Halas, and P. Nordlander, Science **302**, 419 (2003).

[30] J. J. Penninkhof, L. A. Sweatlock, A. Moroz, H. A. Atwater, A. van Blaaderen, and A. Polman, J. Appl. Phys. **103**, 123105 (2008).

[31] J. H. Woodruff, J. B. Ratchford, I. A. Goldthorpe, P. C. McIntyre, and C. E. D. Chidsey, Nano Lett. **7**, 1637 (2007).

[32] L. Bauer and E. L. Edward, SIAM J. Appl. Math. **35**, 508 (1978).

[33] H. R. Philipp and E. A. Taft, Phys. Rev. **113**, 1002 (1959).

[34] P. B. Johnson and R. W. Christy, Phys. Rev. B **6**, 4370 (1972).